JACS
JOURNAL OF THE AMERICAN CHEMICAL SOCIETY
pubs.acs.org/JACS
Article

A Quasi-Ordered Mn-Rich Cathode with Highly Reversible Oxygen Anion Redox Chemistry

Weiyuan Huang,[†] Jimin Qiu,[†] Zengqing Zhuo, Jianguo Wen, Yaqing Guo, Yifei Yuan, Zhefeng Chen, Jiangtao Hu, Tianyi Li, Lirong Zheng, Lunhua He, Jinghua Guo, Mingjian Zhang,* Feng Pan,* Khalil Amine,* and Tongchao Liu*

Cite This: *J. Am. Chem. Soc.* 2025, 147, 26218−26225

ABSTRACT: Anionic oxygen redox chemistry in Li-rich Mn-based layer oxide cathodes represents a transformative approach for boosting the energy density of next-generation lithium-ion batteries. However, conventional oxygen redox reactions often induce oxygen dimerization at high voltages, leading to irreversible lattice oxygen loss and a rapid voltage fade. Herein, we achieve highly reversible oxygen redox chemistry through a new quasi-ordered structural design that incorporates both intra- and interlayer cation disorder configurations. This unique structure significantly enhances lattice oxygen stability, effectively stabilizes oxidized oxygen, and inhibits the formation of peroxo- or superoxol-like species, thereby enabling anionic redox reactions to proceed reversibly even at deep delithiation states. The quasi-ordered design mitigates irreversible phase transitions and preserves the structural integrity throughout extended cycling. Consequently, the proposed cathode demonstrates exceptional cyclability with negligible capacity and voltage fade, retaining 99% capacity and 98% average voltage after long-term cycling. This work provides fresh insights into addressing issues related to lattice oxygen instabilities and reforming strategies for developing long-life, high-energy-density anionic redox cathode materials for advanced batteries.

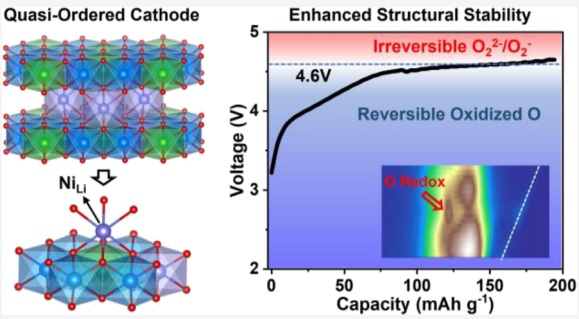

■ INTRODUCTION

The limited capacity of conventional cathodes poses a significant bottleneck in the development of high-energy-density Li-ion batteries, which are essential for long-range electric vehicle technologies.[1] Achieving high reversible capacity requires a delicate balance of substantial redox center activity and sufficient Li^+ storage active sites to facilitate reversible Li^+ insertion and extraction within the structural framework.[2] Compared to conventional layered oxide cathodes that mainly relies on transition metal (TM) redox for capacity, Li-rich Mn-based cathodes incorporate cationic and anionic redox reactions with Li^+ storing in both the Li and TM slabs simutaneously.[3,4] The Li−O−Li special configurations (nonbonding O) in Li-rich cathodes position the O 2p states near the top of the valence band, making oxygen oxidation thermodynamically accessible and enabling substantial capacity contributions from oxygen redox during cycling.[5,6] However, these extra capacities from oxygen redox reactions often come at the expense of voltage stability and capacity retention,[7] which not only shorten cycle life but also complicates battery management, hindering their large-scale practical deployment.

The instability of oxygen redox chemistry is primarily associated with Li-rich ordered configuration, where abundant and spatially proximate nonbonding O atoms increase susceptibility to oxygen loss and irreversible TM migration toward TM dense phases.[8] Specifically, in Li-rich domains with localized $LiMn_6$ honeycomb superstructure ordering, TM migration is thermodynamically favorable during delithiation, creating intralayer vacancies and initiating the formation of low-coordination oxidized oxygen species.[9,10] Locally enriched oxidized O species often aggregate and dimerize, forming peroxo- and superoxo-like species and even oxygen molecules,[4,11] which subsequently escapes from the lattice, leading to irreversible structural degradation and nanovoid formation.[12] Efforts to mitigate lattice oxygen instability during cycling have included strategies such as increasing the TM migration barrier through modified interlayer stacking[13,14] or constructing ordered TM ribbon or mesh structures within the TM layers to spatially separate oxidized oxygen.[10,15] Specifically, in O_2-type Li-rich cathodes, structural stability originates from the specific lattice stacking sequence, where intralayer TM migration is thermodynamically suppressed due to strong repulsion between face-sharing cations.[13,16] This suppression

Received: February 22, 2025
Revised: June 25, 2025
Accepted: June 26, 2025
Published: July 15, 2025

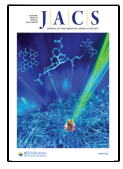

https://doi.org/10.1021/jacs.5c03271
J. Am. Chem. Soc. 2025, 147, 26218−26225

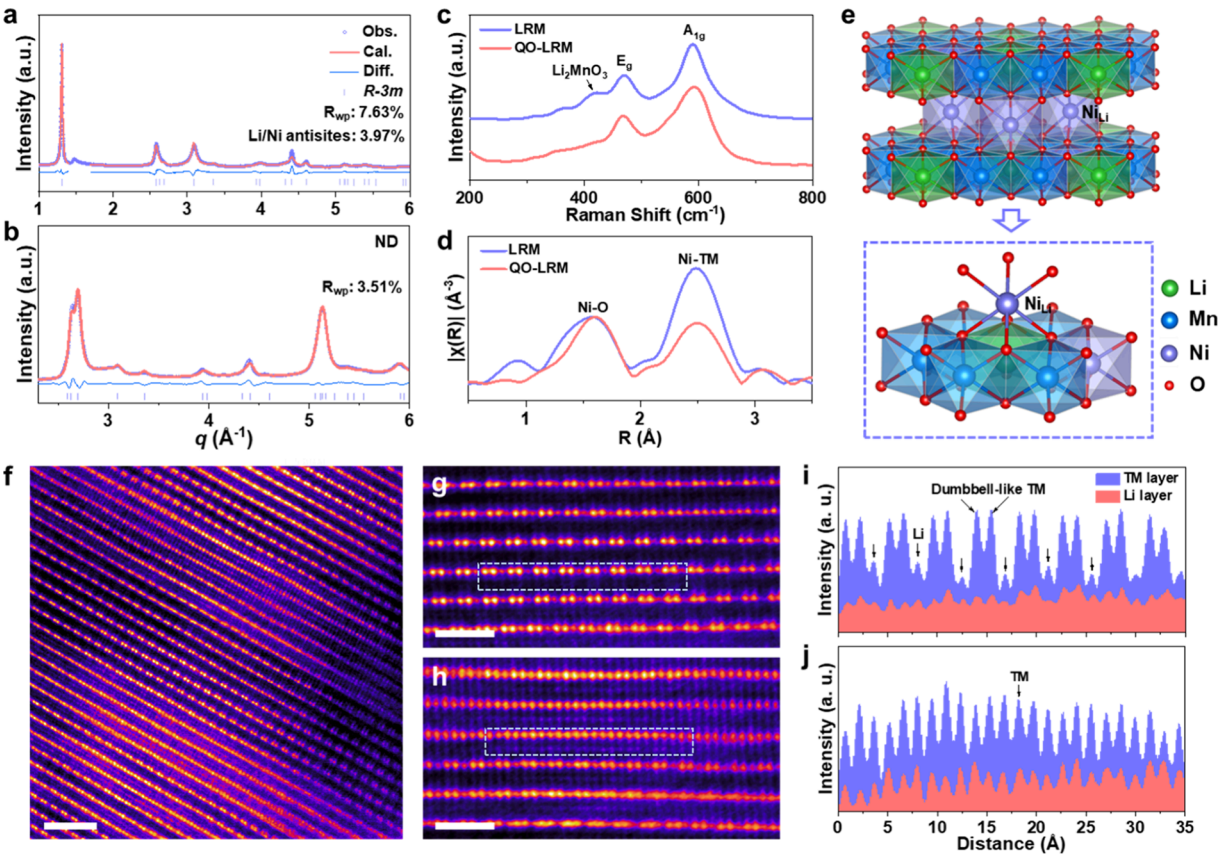

Figure 1. Structural characterization of the QO-LRM cathode. Combined Rietveld refinement of X-ray diffraction (a) and neutron diffraction (b) patterns for QO-LRM. (c) Raman spectra of QO-LRM and LRM. (d) FT-EXAFS at the Ni K-edge, illustrating local structural environments in QO-LRM and LRM. (e) Schematic diagram of the quasi-ordered structure configuration. (f) HAADF-STEM images showing the atomic arrangement of QO-LRM. Scale bar: 1 nm. Enlarged views highlighting the Li-rich (g) and $LiTMO_2$ (h) structures. Scale bars: 0.5 nm. (i, j) Atomic intensity distribution along the selected columns marked by dashed rectangles in (g) and (h), respectively.

facilitates reversible TM migration and enhances the structural robustness during cycling. While these approaches improve electrochemical performance to some extent, they have not yet prevented structural instability during prolonged cycling. Another concept like disordered rock-salt cathodes can disrupt TM/Li ordering and maintain substantial oxygen redox for ultrahigh capacity. However, these materials still experience significant oxygen loss and irreversible cation rearrangement, which damages Li diffusion percolation paths and leads to rapid capacity and voltage fade.[17] Therefore, the state-of-the-art material paradigm fails to overcome the intrinsic instability of lattice oxygen redox, necessitating the leverage of new material science principles to create a stable local lattice oxygen binding environment.

Beyond typical Li-rich cathodes, we introduce a new Co-free Li-rich Mn-based quasi-ordered layered structure cathode (QO-LRM) in this work, featuring both intra- and interlayer cation disorder configurations to address the long-standing challenge of lattice oxygen instability-induced electrochemical decay. The unique structural design, featuring a short-range, partially Ni-substituted intralayer $LiMn_6$ honeycomb superstructure and a high degree of interlayer cation disorder, effectively mitigates the formation of peroxo- or superoxol-like species and facilitates reversible anionic redox. This innovation extends the upper voltage and utilization limit for reversible lattice oxygen reactions, delivering over three times the reversible oxygen anion redox capacity of conventional Li-rich cathodes while maintaining exceptional lattice oxygen stability and structural integrity over long-term cycling. Consequently, the designed QO-LRM cathode demonstrates a high capacity of 262 mAh g^{-1} with ultrastable O redox chemistry, showing negligible capacity and voltage decay, with a capacity retention of 99% and a voltage retention of 98% after 100 cycles. This work establishes a promising framework for rational structure design to achieve high-performance anionic redox cathodes for next-generation batteries.

■ RESULTS AND DISCUSSION

Characterization of the Quasi-Ordered Structure Design. The QO-LRM material was prepared by coprecipitation followed by a molten salt procedure (see Experimental section in the Supporting Information). The chemical composition was determined to be $Li_{0.88}Mn_{0.72}Ni_{0.13}O_2$ by inductively coupled plasma-optical emission spectroscopy (ICP-OES, Table S1). Powder X-ray diffraction (XRD) and neutron diffraction (ND) were employed to characterize the lattice structure of the QO-LRM cathode. Figure 1a,b shows characteristic Bragg diffraction peaks indicative of a well-defined layered structure of the *R*-3*m* space group, with additional superlattice peaks at around q = 1.5 Å corresponding to the honeycomb $LiMn_6$ superstructure units in the TM layers. The combined refinement results of XRD and ND reveal that QO-LRM contains 3.97% of the Li/TM disorder (Tables S2 and S3), which is significantly higher than that of

https://doi.org/10.1021/jacs.5c03271
J. Am. Chem. Soc. 2025, 147, 26218−26225

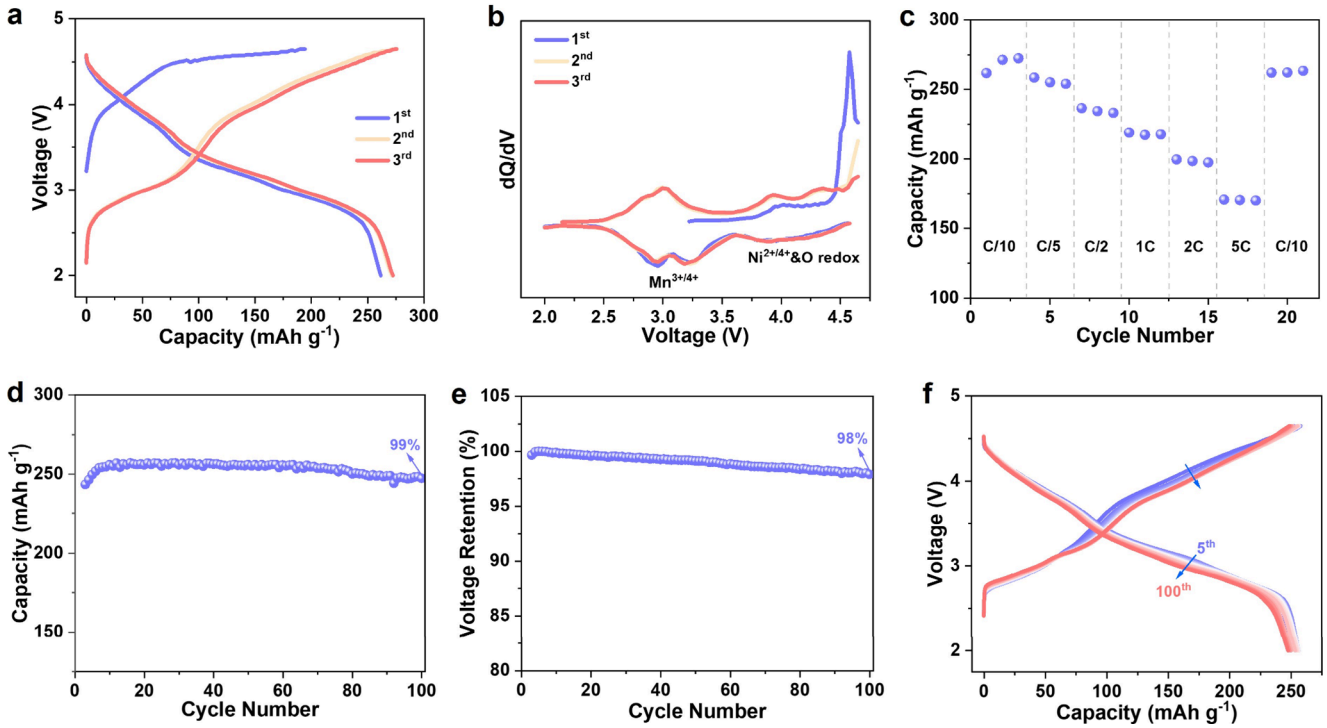

Figure 2. Electrochemical performance of the QO-LRM cathode. (a) Charge−discharge curves of QO-LRM for the first three cycles at a current rate of 0.1C within the voltage range of 2.0−4.65 V. (b) Corresponding dQ/dV profiles for QO-LRM. (c) Rate performance of the QO-LRM cathode. Capacity stability (d) and average voltage stability (e) of QO-LRM at 0.2C. (f) Charge−discharge profiles of QO-LRM from the 5th to the 100th cycle at a current rate of 0.2C.

0.89% in $Li_{1.2}Mn_{0.6}Ni_{0.2}O_2$ (denoted as LRM, Figure S1 and Tables S4 and S5), a typical Co-free Li-rich Mn-based cathode, demonstrating a pronounced interlayer disordered arrangement of cations. Additionally, the QO-LRM cathode exhibits a broadened superstructure peak with reduced peak intensity compared to that of the LRM cathode (Figure S2), which is attributed to superlattice structure distortion and stacking faults. Raman spectroscopy was performed to further investigate the local structural characteristics (Figure 1c). Specifically, two peaks around 470 and 590 cm^{-1} represent the E_g and A_{1g} vibrations of the $LiTMO_2$-type layered structure, respectively.[18] The peak around 416 cm^{-1} in the spectrum of LRM is identified as the fingerprint of the Li_2MnO_3-like phase,[18,19] which significantly decreases in QO-LRM, aligning with the XRD and ND results and confirming the intralayer disorder structure with substantial decrease in long-range order of honeycomb superlattice within the QO-LRM cathode. Fourier transform extended X-ray absorption fine structures (FT-EXAFS) further examined the local structure configurations of QO-LRM and LRM (Figure 1d). No significant differences were observed in the Mn−O and Mn−TM peak intensities (Figure S3), while QO-LRM exhibited a much lower intensity in the Ni−TM peak compared to LRM, indicating the intralayer Ni replacement of Mn in $LiMn_6$ superstructure units. Density functional theory (DFT) calculations suggest that Ni substitution in the $LiMn_6$ superstructure increases the oxygen vacancy formation energy at deep delithiated states (Figure S4 and Table S6).

High-angle annular dark-field scanning transmission electron microscopy (HAADF-STEM) was conducted to visualize the lattice structure at the atomic scale. Figure 1f presents the atomic arrangement of the QO-LRM, with enlarged views of Li-rich and $LiTMO_2$ structures displayed in Figure 1g and Figure 1h, respectively. The QO-LRM shows a discretely distributed dumbbell atomic arrangement, separated by long-range bright spot columns, with additional bright spot columns observed between adjacent two-atom dumbbells. Intensity profiles along selected atomic regions (highlighted in Figure 1g) reveal a clear atomic intensity signal between dumbbell atoms in the QO-LRM (Figure 1i). Moreover, obvious Li/TM disordering was observed in QO-LRM, as some atomic intensities appear within the Li layers of both Li-rich and $LiTMO_2$ structures (Figure 1i,j). Similar phenomena were also observed along the [010] direction (Figure S5). High-resolution energy dispersive spectrometry (EDS) analysis revealed a greater Ni distribution in the interlayer disordering regions (Figure S6), suggesting that the lattice disorder is linked to the Ni distribution. In contrast, LRM exhibited an ordered layered structure with a long-range two-atom dumbbell arrangement, signifying the existence of localized $LiMn_6$ superstructure domains in the TM layers (Figure S7). No obvious interlayered disordering was observed in LRM. In general, the comprehensive characterizations reveal that the QO-LRM cathode exhibits a quasi-ordered layered structure with intra- and interlayer cation redistribution (Figure 1e), which is anticipated to reconfigure lattice oxygen environment and ultimately enhances oxygen redox stability.

Enhanced Electrochemical Performance. Electrochemical tests of LRM and QO-LRM cathodes were performed galvanostatically within the voltage range of 2−4.65 V. As shown in Figure 2a, QO-LRM exhibits an initial charge capacity of 194 mAh g^{-1} and a much higher discharge capacity of 262 mAh g^{-1} at 0.1C (1C = 250 mAh g^{-1}), attributing to its Li-deficient nature. Figure 2b presents the results of dQ/dV plots during the first three cycles, which provide insights into the redox mechanism. A high-intensity peak during the first

https://doi.org/10.1021/jacs.5c03271
J. Am. Chem. Soc. 2025, 147, 26218−26225

charge can be assigned to the initial activation process of the Li-rich structure. A broad reductive hump at 3.6−4.5 V is observed, which results from the partial overlap of cationic $Ni^{2+/4+}$ and anionic oxygen redox. In comparison, the LRM delivers a lower discharge capacity of 213 mAh g^{-1} (Figure S8a). The rate capability was further evaluated from 0.1 to 5C. QO-LRM exhibits higher capacities of 237 mAh g^{-1} at 0.5C and 171 mAh g^{-1} at 5C (Figure 2c), compared to 207 and 113 mAh g^{-1} for LRM (Figure S8b). Regarding long-term cycling performance, QO-LRM demonstrates superior capacity and average voltage stability, as expected, achieving 99% capacity retention and 98% voltage retention (voltage decay of 0.46 mV per cycle) after 100 cycles at 0.2C (Figure 2d,e and Figure S9). This performance is notably superior to that of LRM, which shows 80% capacity retention and 90% voltage retention (voltage decay of 3.71 mV per cycle, Figure S10a−c). These results are confirmed by the corresponding charge−discharge profiles and dQ/dV curves of the QO-LRM (Figure 2f and Figure S11) and LRM cathodes (Figure S10d,e). Overall, QO-LRM shows superior electrochemical stability and rate capability compared to prevalence Li-rich cathodes, Co-free LRM, and Co-containing $Li_{1.2}Mn_{0.54}Ni_{0.13}Co_{0.13}O_2$ (LRM-NMC, Figures S12 and S13), owing to the enhanced oxygen redox stability arising from the designed quasi-ordered structure.

Quasi-Ordered Design Enables Reversible Structural Evolution and Oxygen Redox Reactions. To unveil the lattice structure evolution of QO-LRM upon cycling, in situ XRD measurements were performed during the initial two cycles. As shown in Figure 3a, the (003) peak of QO-LRM continuously shifts to higher angles during the first charge and to lower angles during discharge, corresponding to lattice shrinkage upon charging and lattice expansion during discharge along the *c*-axis, while the changes along the *a*-axis demonstrate an opposite trend. These abnormal structural changes are associated with the hybridized cationic−anionic redox behaviors in the quasi-ordered structure. Remarkably, QO-LRM maintains its original lattice structure after the initial activation, exhibiting a similar structural evolution in the second cycle as in the first cycle, which highlights its exceptional stability in both lattice structure and chemistry. This is distinguishing from conventional Li-rich cathodes, which show inverse lattice parameter changes during the initial charge process and remain nearly unchanged beyond 4.5 V with the participation of oxygen oxidation (Figure S14). Additionally, the LRM presents significantly different peak shifts in subsequent cycles compared to the first cycle, indicating that the original LRM transforms into a new structure after initial activation and undergoes continuous lattice degradation during further cycling.

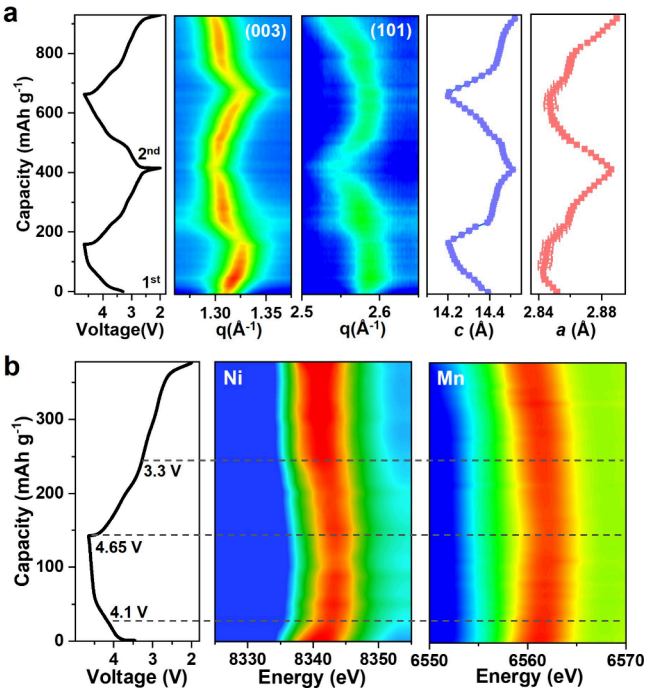

Figure 3. Structural and chemical state evolution of QO-LRM during cycling. (a) In situ XRD patterns showing variations in the (003) and (101) Bragg peaks, along with the refined lattice parameter changes for the QO-LRM cathode during the first two cycles. (b) In situ XANES spectra of Ni K and Mn K-edges for QO-LRM.

To elucidate the charge compensation mechanisms in the QO-LRM cathode, in situ X-ray absorption near edge spectroscopy (XANES) was used to track the chemical state variations of TMs during the charge and discharge processes. As shown in Figure 3b, QO-LRM shows a positive shift of the Ni K-edge, implying Ni oxidation as Li^+ extraction. No significant Ni K-edge shift is observed upon charging above 4.1 V, indicating that oxygen redox participation occurs. After discharging below 3.3 V, the negligible shift in the Ni K-edge suggests that the low voltage capacity in QO-LRM predominantly arises from $Mn^{4+/3+}$ redox reactions during discharge. For LRM, the Ni edge shift becomes much slower when charged above 4.5 V, which can be ascribed to the involvement of oxygen oxidation reactions in charge compensation at this stage (Figure S15). Regarding Mn, slight edge changes are detected due to local structural variations, as Mn is nearly in the +4 valence state in the pristine state and cannot be further oxidized.

Given the critical role of oxygen redox reactions in the charge compensation mechanism, mapping of resonant inelastic X-ray scattering (mRIXS) was employed as a sensitive and reliable method to probe oxygen oxidation states and investigate oxygen chemistry. As presented in Figure 4a and Figure S16, the broad feature around 525.5 eV in emission energy corresponds to O^{2-} states in the pristine LRM. Upon charging to 4.5 and 4.6 V, new features emerge at excitation and emission energies around 531 and 524 eV, as well as the features near the elastic line at 531 eV excitation energy in LRM (indicated by arrows). These features indicate the formation of O_2 dimers,[20] reflecting the oxidation of lattice oxygen from the −2 state to a higher valence state. Here, we use the term 'oxidized O' to specifically refer to lattice oxygen that has undergone oxidation, without implying a defined molecular structure or bonding configuration. In QO-LRM, the oxidized O signal is observed at both 4.4 and 4.6 V (Figure 4b), confirming that oxygen redox is activated at lower voltages and is coupled with cationic redox processes, facilitated by the special quasi-ordered structural configurations. Figure 4c,e presents the soft X-ray absorption spectroscopy (sXAS) spectra of O K-edge in the total fluorescence yield (TFY) mode for LRM and QO-LRM cathodes at various charge states. The pre-edge peaks below 534 eV correspond to the transitions from occupied O 1s orbitals to unoccupied hybridized TM 3d and O 2p orbitals, while the broad peaks above 534 eV are attributed to the transitions to hybridized states TM 4sp and O 2p

https://doi.org/10.1021/jacs.5c03271
J. Am. Chem. Soc. 2025, 147, 26218−26225

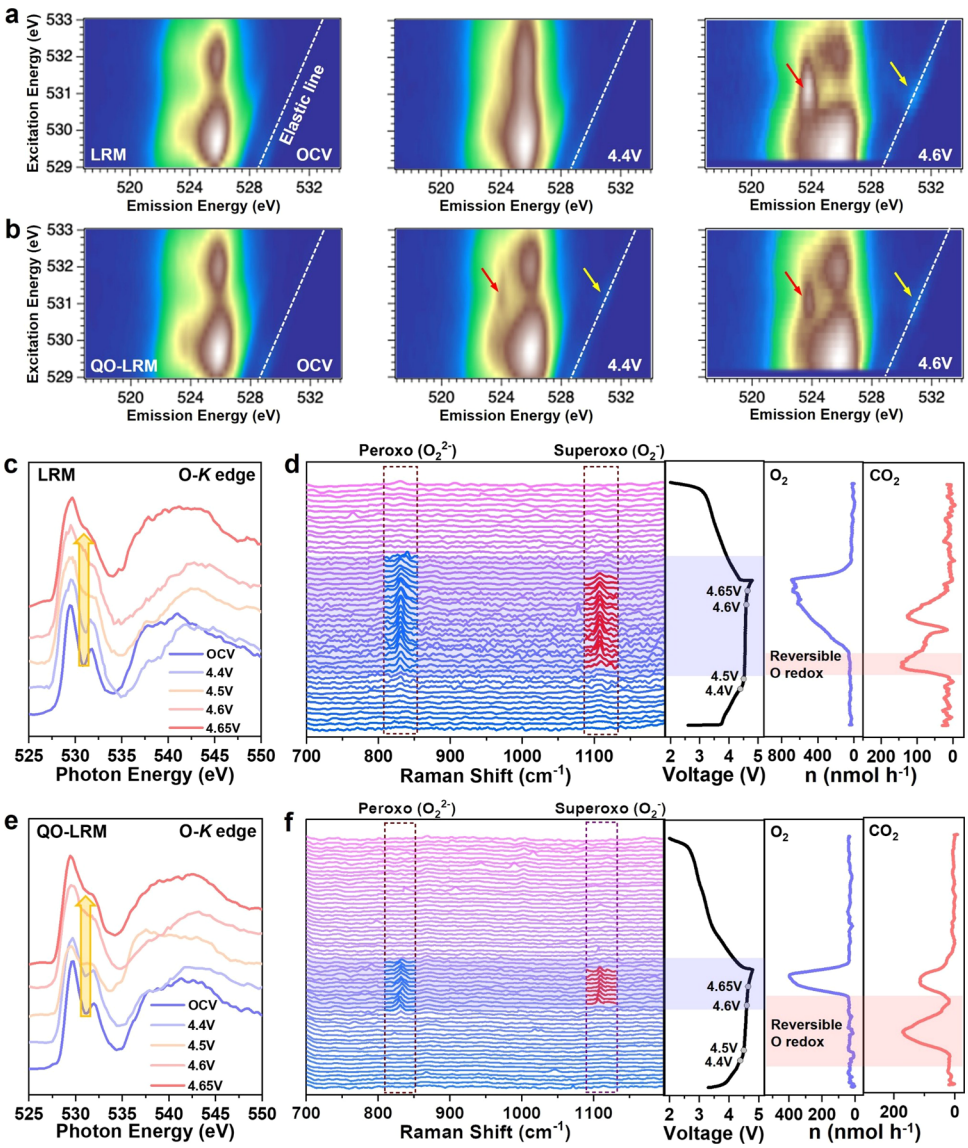

Figure 4. Oxygen anion redox behavior of QO-LRM. O−K mRIXS images of LRM (a) and QO-LRM (b) at OCV, 4.4 V, and 4.6 V, with arrows highlighting features associated with O_2 dimer formation, reflecting the oxidation of lattice oxygen. O−K sXAS spectra of LRM (c) and QO-LRM (e) at OCV, 4.4 V, 4.5 V, 4.6 V, and 4.65 V. The arrows highlight the increase in integrated intensity of the sXAS profiles. In situ Raman and DEMS measurements for LRM (d) and QO-LRM (f).

orbitals. In QO-LRM, the integrated intensity of the pre-edge peaks increases progressively from OCV to 4.4, 4.5, 4.6, and 4.65 V, corresponding to an increasing density of the oxidized O states.[5,21]

To further investigate the real-time lattice oxygen evolution, we conducted in situ shell-isolated nanoparticle-enhanced Raman spectroscopy (SHINES). In Figure 4d, new peaks at around 830 and 1120 cm^{-1} appear in LRM when charged to approximately 4.5 V, indicating the formation of peroxo (O_2^{2-})- and superoxo (O_2^-)-like species with an extended O−O distance.[22] In contrast, no detectable signals of either an O_2^{2-} or an O_2^--like species are observed in QO-LRM until the charging voltage exceeds 4.6 V (Figure 4f). This delayed appearance, despite clear oxidized O signals in mRIXS at 4.4 V, signifies that O^{2-} is initially oxidized without the immediate formation of O_2^{2-}/O_2^--like species, while the subsequent generation of O_2^{2-}/O_2^--like species is significantly delayed by the quasi-ordered design. The unstable lattice oxygen oxidized products, such as O_2^{2-}- and O_2^--like species, are prone to transform into O_2 gas. In situ differential electrochemical mass spectrometry (DEMS) was performed to detect the gas evolution during cycling. The O_2 release can be related to the lattice oxygen loss, while CO_2 is primarily attributed to the decomposition of the carbonated electrolyte. We refer to the region starting from the oxygen redox activation before O_2 gas release as the reversible O redox band, as highlighted in Figure 4d,f. It is observed that the release of the O_2 signal is significantly delayed in QO-LRM and is released in a smaller amount compared to LRM, further confirming the inhibition of irreversible lattice oxygen loss. The capacity contribution from reversible redox in QO-LRM is more than three times higher than that in conventional LRM. This elevation of the oxidation state limit provides vast potential for fully utilizing reversible anionic redox reactions, benefiting from the unique quasi-ordered structural design, which effectively optimizes the configuration of lattice oxygen, thereby preventing its undesired transformation into unstable O_2^{2-}/O_2^--like species and greatly improving structural stability.

https://doi.org/10.1021/jacs.5c03271
J. Am. Chem. Soc. 2025, 147, 26218−26225

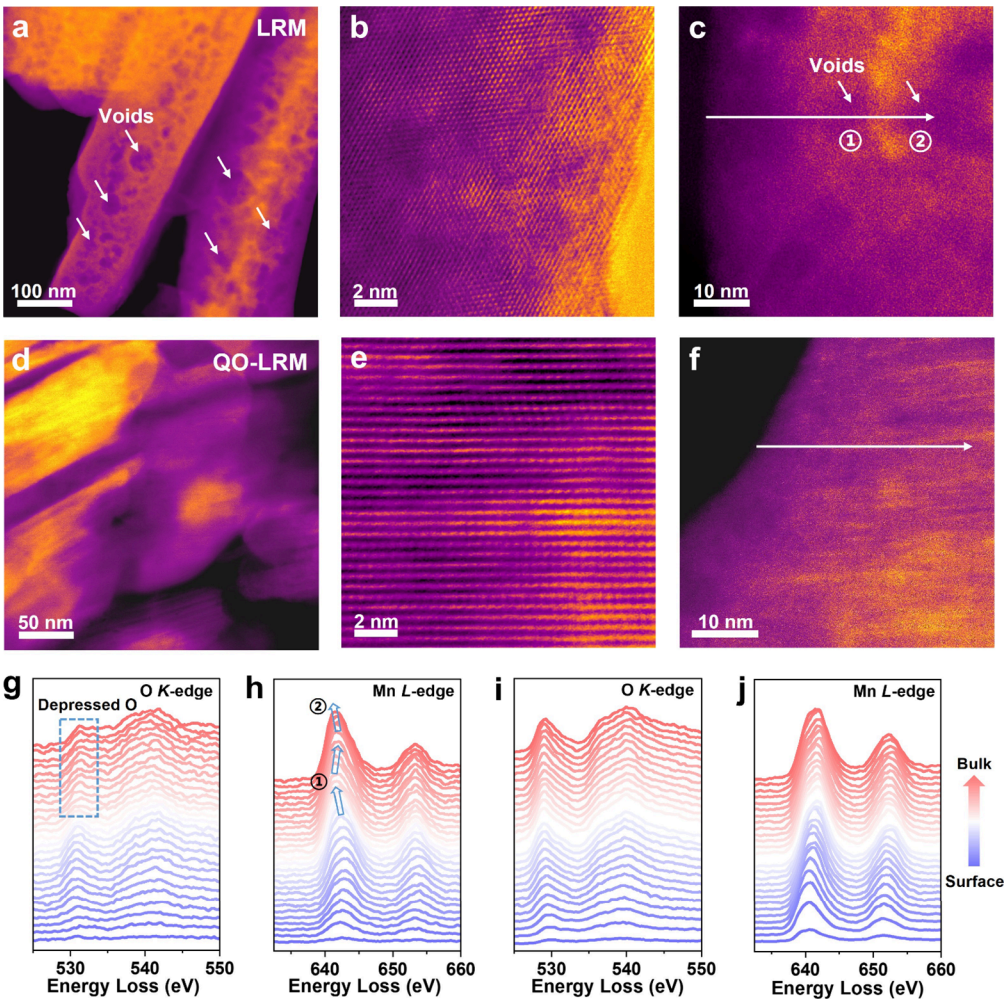

Figure 5. Enhanced structural stability of QO-LRM. HAADF-STEM images showing the morphology of LRM (a) and QO-LRM (d) cathodes after 100 cycles, with nanovoids indicated by arrows in (a). Atomic-resolution HAADF-STEM images revealing the presence of the retained layered structure with dumbbell-like TM configurations in QO-LRM (e), compared to LRM with a rock-salt structure (b). EELS line scans from the surface to bulk are indicated by arrows in LRM (c) and QO-LRM (f). O K-edge and Mn L-edge EELS spectra of LRM (g, h) and QO-LRM (i, j) cathodes. The reduced O K-edge intensity is highlighted in (g) and the lower Mn L-edge peak energy in nanovoid regions of LRM is shown in (h).

Enhanced Structural Stability. To explore the intricate connection between oxygen redox chemistry and structural stability, the HAADF-STEM technique was adopted to conduct structural examination at nano and atomic scales after 100 cycles. Figure 5a presents the nanovoid formation across the entire particles in the cycled LRM cathode. Atomic-resolution STEM imaging further verifies a transformation of the surface structure into a rock-salt phase (Figure 5b). By coupling HAADF-STEM imaging with electron energy loss spectroscopy (EELS) analysis, we confirm that the nanovoids arise due to irreversible lattice oxygen loss, as evidenced by the depressed oxygen peak and Mn reduction in both the surface and bulk nanovoid regions (Figure 5c,g,h). These irreversible oxygen losses and phase transitions greatly contribute to the capacity and voltage decay in LRM cathodes. In contrast, the cycled QO-LRM cathode maintains its morphological integrity, showing no noticeable nanovoid formation (Figure 5d). Remarkably, clear layered lattice fringes with intralayer dumbbell configurations are still visible in the bulk, even after extended cycling (Figure 5e), indicating minimal TM migration and negligible irreversible structural degradation. EELS results reveal a relatively uniform distribution of the polarized O and Mn chemical states in the bulk (Figure 5f,i,j), with lower polarized O intensity and Mn valence states at the surface attributed to the inevitable interfacial side reactions. These findings demonstrate that the unique quasi-ordered structure design of QO-LRM provides an exceptionally stable lattice framework, which correlates with highly reversible oxygen redox chemistry and contributes to the impressive cycling performance.

■ CONCLUSIONS

The introduction of anionic redox reactions endows Li-rich cathode systems with ultrahigh capacity, but this comes at the cost of rapid structural degradation and electrochemical decay due to lattice oxygen instability. This has reinforced the long-standing belief that oxidized lattice oxygen is thermodynamically unstable and inherently correlates with poor electrochemical reversibility, blocking the utilization of oxygen redox chemistry. Excitedly, in this work, we reveal that the reversibility of oxygen redox is not directly related to the extent of lattice oxygen oxidation; instead, it is highly associated with lattice configurations. By developing a quasi-ordered structural design strategy, we effectively stabilize lattice

https://doi.org/10.1021/jacs.5c03271
J. Am. Chem. Soc. 2025, 147, 26218−26225

oxidized O species and inhibit the formation of O_2^{2-}/O_2^{-}-like species that trigger irreversible lattice O loss. This strategy significantly elevates the upper utilization limit of reversible oxygen redox, enabling the simultaneous achievement of high capacity with virtually no voltage decay—demonstrated by 98% average voltage retention over 100 cycles with only 0.46 mV voltage decay per cycle, which is approximately an order of magnitude lower than that observed in conventional Li-rich cathodes. These findings represent a breakthrough in understanding and enhancing the stability of anionic redox chemistry, paving the way for the development of cathodes with higher energy density and long lifespan.

■ ASSOCIATED CONTENT

Supporting Information

The Supporting Information is available free of charge at https://pubs.acs.org/doi/10.1021/jacs.5c03271.

Experimental procedures and additional data include XRD patterns, ND patterns, HAADF-STEM images, EDS mappings, XANES spectra, EXAFS spectra, mRIXS intensity cut patterns, and electrochemical performance data (PDF)

■ AUTHOR INFORMATION

Corresponding Authors

Mingjian Zhang − *School of Science and Engineering, The Chinese University of Hong Kong, Shenzhen 518172, China*; Email: zhangmingjian@cuhk.edu.cn

Feng Pan − *School of Advanced Materials, Peking University, Shenzhen Graduate School, Shenzhen 518055, China*; orcid.org/0000-0002-8216-1339; Email: panfeng@pkusz.edu.cn

Khalil Amine − *Chemical Sciences and Engineering Division, Argonne National Laboratory, Lemont, Illinois 60439, United States*; orcid.org/0000-0001-9206-3719; Email: amine@anl.gov

Tongchao Liu − *Chemical Sciences and Engineering Division, Argonne National Laboratory, Lemont, Illinois 60439, United States*; orcid.org/0000-0002-6010-3891; Email: liut@anl.gov

Authors

Weiyuan Huang − *Chemical Sciences and Engineering Division, Argonne National Laboratory, Lemont, Illinois 60439, United States*

Jimin Qiu − *School of Advanced Materials, Peking University, Shenzhen Graduate School, Shenzhen 518055, China*

Zengqing Zhuo − *Advanced Light Source, Lawrence Berkeley National Laboratory, Berkeley, California 94720, United States*; orcid.org/0000-0001-6602-760X

Jianguo Wen − *Center for Nanoscale Materials, Argonne National Laboratory, Lemont, Illinois 60439, United States*; orcid.org/0000-0002-3755-0044

Yaqing Guo − *College of Chemistry and Materials Engineering, Wenzhou University, Wenzhou, Zhejiang 325035, China*

Yifei Yuan − *College of Chemistry and Materials Engineering, Wenzhou University, Wenzhou, Zhejiang 325035, China*; orcid.org/0000-0002-2360-8794

Zhefeng Chen − *School of Advanced Materials, Peking University, Shenzhen Graduate School, Shenzhen 518055, China*

Jiangtao Hu − *College of Chemistry and Environmental Engineering, Shenzhen University, Shenzhen 518060, China*; orcid.org/0000-0002-2725-7581

Tianyi Li − *X-ray Science Division, Argonne National Laboratory, Lemont, Illinois 60439, United States*; orcid.org/0000-0002-6234-6096

Lirong Zheng − *Beijing Synchrotron Radiation Facility, Institute of High Energy Physics, Chinese Academy of Sciences, Beijing 100049, China*

Lunhua He − *Spallation Neutron Source Science Center, Dongguan 523803, China*

Jinghua Guo − *Advanced Light Source, Lawrence Berkeley National Laboratory, Berkeley, California 94720, United States*; orcid.org/0000-0002-8576-2172

Complete contact information is available at: https://pubs.acs.org/10.1021/jacs.5c03271

Author Contributions

[†]W.H. and J.Q. contributed equally to this work.

Notes

The authors declare no competing financial interest.

■ ACKNOWLEDGMENTS

This work gratefully acknowledges support from the U.S. Department of Energy (DOE), Office of Energy Efficiency and Renewable Energy, Vehicle Technologies Office. Argonne National Laboratory is operated for DOE, Office of Science by UChicago Argonne, LLC, under contract number DE-AC02-06CH11357. This research used resources of the Advanced Photon Source (11-ID-C and 17-BM), a U.S. Department of Energy (DOE) Office of Science user facility operated for the DOE Office of Science by Argonne National Laboratory under contract no. DE-AC02-06CH11357. This work was performed, in part, at the Center for Nanoscale Materials, an Office of Science user facility, supported by the U.S. Department of Energy, Office of Science, Office of Basic Energy Sciences, under contract no. DE-AC02-06CH11357. This research used resources of the Advanced Light Source, which is a DOE Office of Science user facility under contract no. DE-AC02-05CH11231. This work was supported by the National Natural Science Foundation of China (52172175), the Program from Guangdong Introducing Innovative and Entrepreneurial Teams (2019ZT08L101 and RCTDPT-2020-001), and the Shenzhen Science and Technology Research Grant (JCYJ20210324130812033). This work acknowledges the Major Science and Technology Infrastructure Project of Material Genome Big-Science Facilities Platform supported by the Municipal Development and Reform Commission of Shenzhen, Basic and Applied Basic Research Foundation of Guangdong Province (no. 2021B1515130002), International Joint Research Center for Electric Vehicle Power Battery and Materials (no. 2015B01015), Guangdong Key Laboratory of Design and Calculation of New Energy Materials (no. 2017B030301013), and Shenzhen Key Laboratory of New Energy Resources Genome Preparation and Testing (no. ZDSYS201707281026184).

■ REFERENCES

(1) Tarascon, J. M.; Armand, M. Issues and challenges facing rechargeable lithium batteries. *Nature* **2001**, *414*, 359−367. Malik, R. Li-rich layered cathode materials: Transition metals in transit. *Joule*

2017, *1* (4), 647−648. Whittingham, M. S. Lithium batteries and cathode materials. *Chem. Rev.* **2004**, *104*, 4271−4301.

(2) Huang, W.; Yang, L.; Chen, Z.; Liu, T.; Ren, G.; Shan, P.; Zhang, B. W.; Chen, S.; Li, S.; Li, J.; et al. Elastic lattice enabling reversible tetrahedral Li storage sites in a high-capacity manganese oxide cathode. *Adv. Mater.* **2022**, *34* (30), No. 2202745.

(3) Li, B.; Zhuo, Z.; Zhang, L.; Iadecola, A.; Gao, X.; Guo, J.; Yang, W.; Morozov, A. V.; Abakumov, A. M.; Tarascon, J. M. Decoupling the roles of Ni and Co in anionic redox activity of Li-rich NMC cathodes. *Nat. Mater.* **2023**, *22* (11), 1370−1379. Zuo, W.; Luo, M.; Liu, X.; Wu, J.; Liu, H.; Li, J.; Winter, M.; Fu, R.; Yang, W.; Yang, Y. Li-rich cathodes for rechargeable Li-based batteries: reaction mechanisms and advanced characterization techniques. *Energy Environ. Sci.* **2020**, *13* (12), 4450−4497.

(4) McCalla, E.; Abakumov, A. M.; Saubanère, M.; Foix, D.; Berg, E. J.; Rousse, G.; Doublet, M. L.; Gonbeau, D.; Novák, P.; Van Tendeloo, G.; Dominko, R.; Tarascon, J. M. Visualization of O-O peroxo-like dimers in high-capacity layered oxides for Li-ion batteries. *Science* **2015**, *350*, 1516−1521.

(5) Luo, K.; Roberts, M. R.; Hao, R.; Guerrini, N.; Pickup, D. M.; Liu, Y. S.; Edstrom, K.; Guo, J.; Chadwick, A. V.; Duda, L. C.; et al. Charge-compensation in 3d-transition-metal-oxide intercalation cathodes through the generation of localized electron holes on oxygen. *Nat. Chem.* **2016**, *8* (7), 684−691.

(6) Seo, D. H.; Lee, J.; Urban, A.; Malik, R.; Kang, S.; Ceder, G. The structural and chemical origin of the oxygen redox activity in layered and cation-disordered Li-excess cathode materials. *Nat. Chem.* **2016**, *8* (7), 692−697.

(7) Hu, E.; Yu, X.; Lin, R.; Bi, X.; Lu, J.; Bak, S.; Nam, K.-W.; Xin, H. L.; Jaye, C.; Fischer, D. A.; et al. Evolution of redox couples in Li- and Mn-rich cathode materials and mitigation of voltage fade by reducing oxygen release. *Nat. Energy* **2018**, *3* (8), 690−698. Myeong, S.; Cho, W.; Jin, W.; Hwang, J.; Yoon, M.; Yoo, Y.; Nam, G.; Jang, H.; Han, J. G.; Choi, N. S.; et al. Understanding voltage decay in lithium-excess layered cathode materials through oxygen-centred structural arrangement. *Nat. Commun.* **2018**, *9* (1), 3285.

(8) Gu, M.; Belharouak, I.; Zheng, J. M.; Wu, H. M.; Xiao, J.; Genc, A.; Amine, K.; Thevuthasan, S.; Baer, D. R.; Zhang, J.-G.; et al. Formation of the spinel phase in the layered composite cathode used in Li-ion batteries. *ACS Nano* **2013**, *7*, 760−767. Csernica, P. M.; Kalirai, S. S.; Gent, W. E.; Lim, K.; Yu, Y.-S.; Liu, Y.; Ahn, S.-J.; Kaeli, E.; Xu, X.; Stone, K. H.; et al. Persistent and partially mobile oxygen vacancies in Li-rich layered oxides. *Nat. Energy* **2021**, *6* (6), 642−652. Zhao, S.; Yan, K.; Zhang, J.; Sun, B.; Wang, G. Reaction mechanisms of layered lithium-rich cathode materials for high-energy lithium-ion batteries. *Angew. Chem., Int. Ed. Engl.* **2021**, *60* (5), 2208−2220.

(9) Kim, B.; Song, J.-H.; Eum, D.; Yu, S.; Oh, K.; Lee, M. H.; Jang, H.-Y.; Kang, K. A theoretical framework for oxygen redox chemistry for sustainable batteries. *Nat. Sustain.* **2022**, *5* (8), 708−716. House, R. A.; Marie, J.-J.; Pérez-Osorio, M. A.; Rees, G. J.; Boivin, E.; Bruce, P. G. The role of O_2 in O-redox cathodes for Li-ion batteries. *Nat. Energy* **2021**, *6* (8), 781−789.

(10) House, R. A.; Maitra, U.; Perez-Osorio, M. A.; Lozano, J. G.; Jin, L.; Somerville, J. W.; Duda, L. C.; Nag, A.; Walters, A.; Zhou, K. J.; et al. Superstructure control of first-cycle voltage hysteresis in oxygen-redox cathodes. *Nature* **2020**, *577* (7791), 502−508.

(11) Sathiya, M.; Rousse, G.; Ramesha, K.; Laisa, C. P.; Vezin, H.; Sougrati, M. T.; Doublet, M. L.; Foix, D.; Gonbeau, D.; Walker, W.; et al. Reversible anionic redox chemistry in high-capacity layered-oxide electrodes. *Nat. Mater.* **2013**, *12* (9), 827−835.

(12) Yan, P.; Zheng, J.; Tang, Z. K.; Devaraj, A.; Chen, G.; Amine, K.; Zhang, J. G.; Liu, L. M.; Wang, C. Injection of oxygen vacancies in the bulk lattice of layered cathodes. *Nat. Nanotechnol.* **2019**, *14* (6), 602−608. Marie, J. J.; House, R. A.; Rees, G. J.; Robertson, A. W.; Jenkins, M.; Chen, J.; Agrestini, S.; Garcia-Fernandez, M.; Zhou, K. J.; Bruce, P. G. Trapped O_2 and the origin of voltage fade in layered Li-rich cathodes. *Nat. Mater.* **2024**, *23* (6), 818−825.

(13) Eum, D.; Kim, B.; Kim, S. J.; Park, H.; Wu, J.; Cho, S. P.; Yoon, G.; Lee, M. H.; Jung, S. K.; Yang, W.; et al. Voltage decay and redox asymmetry mitigation by reversible cation migration in lithium-rich layered oxide electrodes. *Nat. Mater.* **2020**, *19* (4), 419−427.

(14) Luo, D.; Zhu, H.; Xia, Y.; Yin, Z.; Qin, Y.; Li, T.; Zhang, Q.; Gu, L.; Peng, Y.; Zhang, J.; et al. A Li-rich layered oxide cathode with negligible voltage decay. *Nat. Energy* **2023**, *8* (10), 1078−1087.

(15) Gao, A.; Zhang, Q.; Li, X.; Shang, T.; Tang, Z.; Lu, X.; Luo, Y.; Ding, J.; Kan, W. H.; Chen, H.; et al. Topologically protected oxygen redox in a layered manganese oxide cathode for sustainable batteries. *Nat. Sustain.* **2022**, *5* (3), 214−224.

(16) Jang, H.-Y.; Eum, D.; Cho, J.; Lim, J.; Lee, Y.; Song, J.-H.; Park, H.; Kim, B.; Kim, D.-H.; Cho, S.-P.; et al. Structurally robust lithium-rich layered oxides for high-energy and long-lasting cathodes. *Nat. Commun.* **2024**, *15*, 1288.

(17) Huang, J.; Ouyang, B.; Zhang, Y.; Yin, L.; Kwon, D. H.; Cai, Z.; Lun, Z.; Zeng, G.; Balasubramanian, M.; Ceder, G. Inhibiting collective cation migration in Li-rich cathode materials as a strategy to mitigate voltage hysteresis. *Nat. Mater.* **2023**, *22* (3), 353−361. Ji, H.; Wu, J.; Cai, Z.; Liu, J.; Kwon, D.-H.; Kim, H.; Urban, A.; Papp, J. K.; Foley, E.; Tian, Y.; et al. Ultrahigh power and energy density in partially ordered lithium-ion cathode materials. *Nat. Energy* **2020**, *5* (3), 213−221. Li, H.; Fong, R.; Woo, M.; Ahmed, H.; Seo, D.-H.; Malik, R.; Lee, J. Toward high-energy Mn-based disordered-rocksalt Li-ion cathodes. *Joule* **2022**, *6* (1), 53−91.

(18) He, W.; Liu, P.; Qu, B.; Zheng, Z.; Zheng, H.; Deng, P.; Li, P.; Li, S.; Huang, H.; Wang, L.; et al. Uniform Na+ doping-induced defects in Li- and Mn-rich cathodes for high-performance lithium-ion batteries. *Adv. Sci.* **2019**, *6* (14), 1802114. Ji, X.; Xu, Y.; Feng, H.; Wang, P.; Zhou, Y.; Song, J.; Xia, Q.; Tan, Q. Surface $LiMn_{1.4}Ni_{0.5}Mo_{0.1}O_4$ coating and bulk Mo doping of Li-rich Mn-based $Li_{1.2}Mn_{0.54}Ni_{0.13}Co_{0.13}O_2$ cathode with enhanced electrochemical performance for lithium-ion batteries. *ACS Appl. Mater. Interfaces* **2021**, *13* (40), 47659−47670.

(19) Alagar, S.; Ganesan, M.; Karuppiah, C.; Yang, C.-C.; Bagchi, V.; Piraman, S. *ACS Appl. Energy Mater.* **2023**, *6* (2), 622−635.

(20) House, R. A.; Rees, G. J.; Pérez-Osorio, M. A.; Marie, J.-J.; Boivin, E.; Robertson, A. W.; Nag, A.; Garcia-Fernandez, M.; Zhou, K.-J.; Bruce, P. G. First-cycle voltage hysteresis in Li-rich 3*d* cathodes associated with molecular O_2 trapped in the bulk. *Nat. Energy* **2020**, *5*, 777−785. Gao, X.; Li, B.; Kummer, K.; Geondzhian, A.; Aksyonov, D. A.; Dedryvère, R.; Foix, D.; Rousse, G.; Yahia, M. B.; Doublet, M.-L.; Abakumov, A. M.; Tarascon, J.-M. Clarifying the origin of molecular O_2 in cathode oxides. *Nat. Mater.* **2025**, *24*, 743−752.

(21) Yoon, W.-S.; Balasubramanian, M.; Chung, K. Y.; Yang, X.-Q.; McBreen, J.; Grey, C. P.; Fischer, D. A. Investigation of the charge compensation mmechanism on the electrochemically Li-ion deintercalated $Li_{1-x}Co_{1/3}Ni_{1/3}Mn_{1/3}O_2$ electrode system by combination of soft and hard X-ray absorption spectroscopy. *J. Am. Chem. Soc.* **2005**, *127*, 17479−17487.

(22) Zhang, X.; Qiao, Y.; Guo, S.; Jiang, K.; Xu, S.; Xu, H.; Wang, P.; He, P.; Zhou, H. Manganese-based Na-rich materials boost anionic redox in high-performance layered cathodes for sodium-ion batteries. *Adv. Mater.* **2019**, *31* (27), 1807770. Li, X.; Qiao, Y.; Guo, S.; Jiang, K.; Ishida, M.; Zhou, H. A new type of Li-rich rock-salt oxide $Li_2Ni_{1/3}Ru_{2/3}O_3$ with reversible anionic redox chemistry. *Adv. Mater.* **2019**, *31* (11), 1807825.

https://doi.org/10.1021/jacs.5c03271
J. Am. Chem. Soc. 2025, 147, 26218−26225